Journal of Materials Chemistry B

ROYAL SOCIETY OF CHEMISTRY

PAPER

View Article Online
View Journal | View Issue

Cite this: J. Mater. Chem. B, 2023, 11, 5010

3D light-curing printing to construct versatile octopus-bionic patches†

Wen Li,[a] Xiaole Hu,[a] Hongsheng Liu,[a] Jinhuan Tian,[ab] Lihua Li,[ab] Binghong Luo,[ab] Changren Zhou[ab] and Lu Lu *[ab]

Received 20th March 2023,
Accepted 9th May 2023

DOI: 10.1039/d3tb00590a

rsc.li/materials-b

Reliable, fast and switchable gluing modes are critically important in medical adhesives and intelligent climbing robot applications. The octopus-bionic patch has attracted the attention of many scholars. The suction cup structure of the octopus achieves adhesion through differential pressure, showing strong adhesion in both dry and wet environments. However, the construction of the octopus-bionic patch remains limited in terms of adaptability, personalization and mass production. Herein, a composite hydrogel consisting of gelatin methacryloyl (GelMA), polyethylene glycol diacrylate (PEGDA) and acrylamide (AAM) was developed, and a structure mimicking the octopus sucker was constructed by digital light processing (DLP). The obtained octopus-bionic patch has strong adhesion, good biocompatibility and multi-functionality. Compared with the template method in most studies, the octopus-bionic patch constructed by the DLP printing method has the advantages of customizability and low cost. In addition, the DLP printing method endows the patch surface with an octopus-like groove structure for a better bionic effect.

1. Introduction

In nature, animals utilize different adhesion mechanisms.[1,2] There are chemically-derived adhesions, such as those used by mussels, barnacles and worms.[3,4] There are also physical adhesions, such as those used by geckos, parasites, bryozoans and octopuses.[5–10] Chemical adhesion is mainly achieved by secreting mucus containing protein molecules. Mussel adhesion occurs mainly through the secretion of foot filament protein by the foot filament gland, and the catechol in the foot filament protein is chelated with cations in seawater to achieve strong adhesion.[7] Physical adhesion is mainly achieved by pressure difference, microstructures and nanostructures, *etc.*[11–13] Compared with chemical bonding, physical bonding has the advantages of less pollution and reusability.[14] Octopus adhesion is physical adhesion.[15,16] The suction cup structure of the octopus is composed of a funnel and an acetabular cavity.[17] The adhesion mechanism is mainly achieved by the acetabulum suction contraction from the vacuum negative pressure and the good sealing of the funnel part.[18] As a result, octopuses can firmly attach to various objects in both dry and moist environments.

For the construction of octopus biomimetic patches, many researchers have tried template methods.[19] For example, Baik *et al.*[8] fabricated an artificial, reversible and water-resistant adhesive inspired by dome-like protrusions through a template method. Huang *et al.*[20] developed a biocompatible wound patch with selective adhesion and personalized design using a combination of template replication and mask-guided lithography. Baik *et al.*[21] developed a biocompatible and highly reversible skin-adhesive patch through a simple polymer replication method. However, the construction of the octopus-bionic patch by the template method has the problems of cumbersome steps, non-adjustable patch size and inability to achieve personalized customization.

Herein, a multifunctional octopus-bionic patch was constructed by digital light processing (DLP) 3D printing (Fig. 1). A dual-network hydrogel containing gelatin methacryloyl (GelMA), polyethylene glycol diacrylate (PEGDA) and acrylamide (AAM), with good biocompatibility and extracellular matrix-like viscoelasticity, was selected as the patch material.[22–24] Through the layer-by-layer photo-curing 3D printing method, the light-curing inks were cured into an octopus-bionic patch that was consistent with the model. The octopus-bionic patch had good adhesion in wet environments while being customizable, bendable, easy to debond, reusable and versatile.

2. Materials and methods

2.1. Materials

Gelatin (Shanghai Aladdin Biochemical Technology Co., Ltd), methacrylic anhydride (Macklin), polyethylene glycol (Macklin),

[a] Department of Materials Science and Engineering, College of Chemistry and Materials Science, Jinan University, Guangzhou 510632, China. E-mail: tlulu@jnu.edu.cn
[b] Engineering Research Center of Artificial Organs and Materials, Ministry of Education, Guangzhou 510632, China

† Electronic supplementary information (ESI) available. See DOI: https://doi.org/10.1039/d3tb00590a

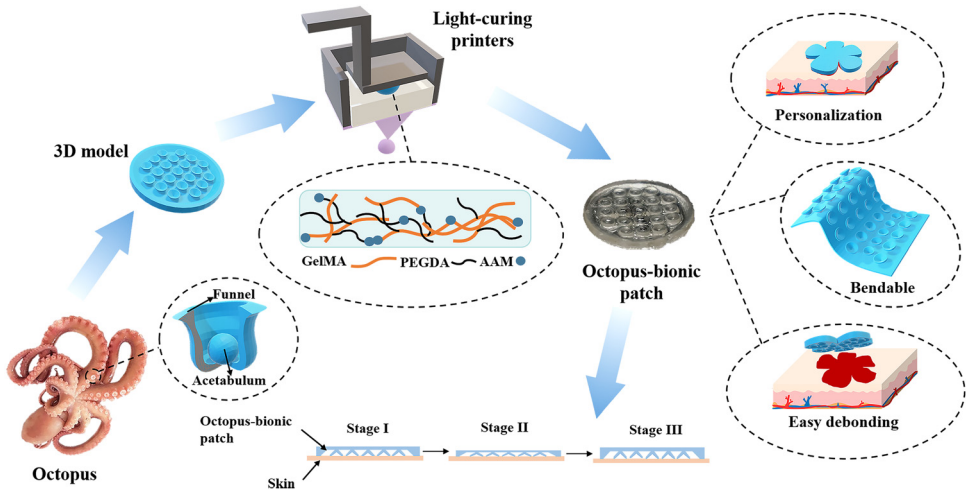

Fig. 1 Schematic diagram of a light-curing printed octopus-bionic patch.

acrylamide (AAM, Macklin), lithium phenyl-2,4,6-trimethylbenzoyl phosphonate (LAP, Bide Pharmatech Co., Ltd), mouse fibroblasts (L929), cell counting kit-8 assay (CCK-8, Biosharp, China), Live/Dead cell staining kit (calcein/propidium iodide double staining kit (AM/PI), keyGEN, China).

2.2. Formulation of light-curing inks

GelMA was synthesized according to a previously described protocol.[25] Briefly, 10 g of gelatin was added to phosphate-buffered saline (PBS) to obtain a 10 wt% solution at 50 °C. Subsequently, 1 mL of methacrylic anhydride was added and the reaction was carried out at 50 °C for 3 hours. After that, 400 mL of deionized water was added. After 1 week of dialysis, it was freeze-dried to obtain spongy GelMA.

PEGDA was synthesized as previously reported.[26] Briefly, 24 g of PEG (M_w = 2000) was dissolved in 72 mL of anhydrous dichloromethane (remove water with calcium hydride), then 0.5 mL of triethylamine was added and 0.9 mL of acryloyl chloride. The reaction was then protected under nitrogen for 48 hours. The resulting solution was then washed with 20 mL of aqueous K_2CO_3 (2 mol L^{-1}) to remove the HCl. Afterwards, the dichloromethane phase was dried with anhydrous $MgSO_4$, centrifuged, and the supernatant was retained and concentrated with ether until a white powder of PEGDA was precipitated. PEGDA with a molecular weight of 1000 and 6000 was also synthesized by the above method.

Light-curing inks were prepared by mixing different concentrations of GelMA, PEGDA and AAM (Table 1), retaining the ink's polymer content at 20 wt%. LAP was added as a photo-initiator at a final concentration of 0.25 wt%. The mixture was shaken carefully until well mixed before storing it in the dark.

Table 1 The proportion of each component in the light-curing inks

Sample	GelMA (wt%)	PEGDA (wt%)	AAM (wt%)
G10 + P10	10	10	0
G10 + P7 + A3	10	7	3
G10 + P5 + A5	10	5	5
G10 + P3 + A7	10	3	7
G10 + A10	10	0	10

2.3. Rheological characterizations

Rheological characterizations were performed on an AR-G2 rheometer (TA Instruments, USA) with a parallel plate (20 mm diameter) geometry and ultraviolet (UV, 320–500 nm) curing accessory for crosslinking the light-curing inks. All rheology tests with UV curing were performed at 25 °C in oscillatory mode at 10 rad s^{-1} and 1% strain with an 800 μm gap. Irradiation intensity was 10 mV cm^{-2}. Frequency sweep tests were carried out from 0.1 to 100 rad s^{-1}. In the frequency sweep tests, the storage (G') and loss (G'') moduli were determined in the regime of linear viscoelasticity (LVE). Strain scans were performed on the hydrogel to demonstrate the LVE range.

2.4. Compression tests

The mechanical properties of the hydrogels were characterized by an electronic universal testing machine (AG-I, SHIMADZU, Japan). The light-curing inks were cured under UV light to form hydrogel cylinders (10 mm in diameter and 3 mm in height). The stress–strain curve was obtained by compressing the sample on an electronic universal testing machine at a speed of 1 mm min^{-1}. And the capability dissipation value was obtained by the closed-loop area of the stress–strain curve.

2.5. Swelling characterizations

Light-curing inks were cured by UV light into hydrogel cylinders (10 mm in diameter and 3 mm in height) and weighed. The hydrogels were immersed in PBS and removed at predetermined time intervals and weighed until there was no further weight change. The swelling ratio of the hydrogel was calculated using the following equation:

$$\text{Swelling ratio} = (M_t - M_0) \div M_0 \times 100\% \quad (1)$$

where M_t: swollen hydrogel weight, M_0: initial hydrogel weight.

Table 2 Material properties of the hydrogel and skin

Material type	Model	Parameters
Hydrogel	Ogden	MU1 = 1.43 × 10^{-3} MPa; ALPHA1 = 16.38 MPa; D1 = 0;
Skin(dermis)[28]	Mooney–Rivlin	C10 = 9.4 kPa; C01 = 82 kPa; D1 = 0

2.6. Biocompatibility

Hydrogel sheets (20 mm in diameter and 400 μm in thickness) were obtained from photocrosslinking light-curing inks. Hydrogel sheets were immersed in PBS for 30 min to remove uncrosslinked monomers and sterilized with 75% alcohol. Then, the hydrogel sheets were placed in 12-well plates. Mouse fibroblasts (L929 cells) were inoculated on the surface of the hydrogel at a cell density of 10^4 cells per well. The culture plate was used as a control group. The cells were cultured at 37 °C and 5% CO_2 for 1, 3, and 5 days. At the selected time point, the viability test was assessed by CCK-8 and a Live/Dead Cell Assay Kit according to the manufacturer's instructions.

2.7. Fabrication of octopus-bionic patches

Computer-Aided Design (CAD) software was used to build octopus-bionic patch models with different shapes and structures. The 3D octopus-bionic patches were obtained by layer-by-layer light-curing ink through a DLP 3D printer (405 nm, 80 W). Printing parameters: layer thickness 0.02 mm, single layer light time 4 s, bottom light time 6 s.

2.8. Normal adhesion test

The adhesion force of the octopus-bionic patch was measured by an electronic universal testing machine. The patch was placed on the upper fixture. A 5 cm × 3.5 cm pork skin was placed on the lower fixture and a layer of the medium (water, 75% alcohol, *etc.*) was applied to the surface of the pork skin (Fig. S5a, ESI†). The patch was attached to the pork skin at a speed of 5 mm min^{-1} and a preload force of 5 N was generated and held for 5 s. The patch was then reverse-stretched at 5 mm min^{-1} until it detached from the pork skin. The force-time curve was obtained. The ratio of the maximum adhesion force to the patch area was the normal adhesion strength.

2.9. Finite element analysis of the adhesion mechanism

The adhesion force of the octopus-bionic patch to the skin was simulated by the finite element simulation software ABAQUS. Due to the nonlinear behavior of the hydrogel material, a hyperelastic material model was used.[27] The stress–strain curve was obtained from the uniaxial compression test of the material and then the simulation was carried out (Fig. S4, ESI†). The following is a table of the obtained material parameters (Table 2).

The small suction cups inside the patch were simulated. The small suction cup was divided into tetrahedral meshes of size 0.1 mm. The skin was fixed and a force of 6 × 10^{-4} N was applied to the top of the small suction cup to deform the small suction cup. The variation curve of the fluid cavity existing between the small suction cup and the skin was obtained.

The octopus-bionic patch was divided into tetrahedral meshes of size 1 mm and the skin was divided into hexahedral meshes of size 2 mm. The contact between the patch and the skin was set as a Lagrangian multiplier with a friction factor of 0.42. The bottom of the skin was fixed and a force of 5 N was applied on the patch. The stress nephogram of the patch was obtained by simulation analysis.

2.10. Statistical analysis

All data are expressed as mean ± standard deviation. The sample size (n) is indicated in the legend of the Experimental

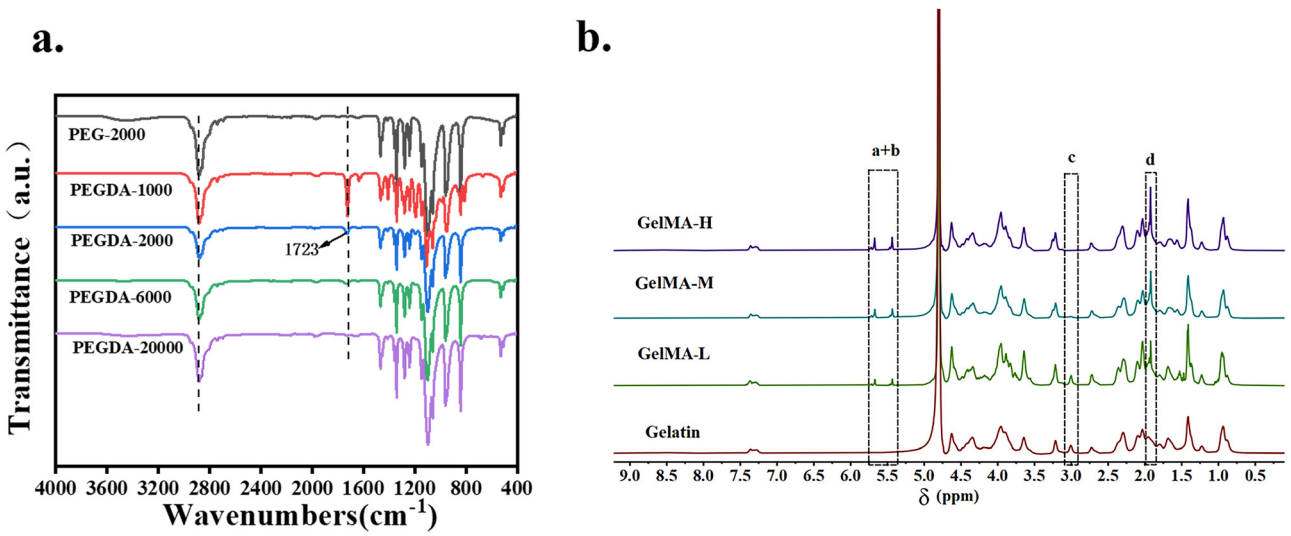

Fig. 2 (a) IR spectra of PEGDA. (b) ^{1}H NMR of GelMA with different degrees of amino substitution.

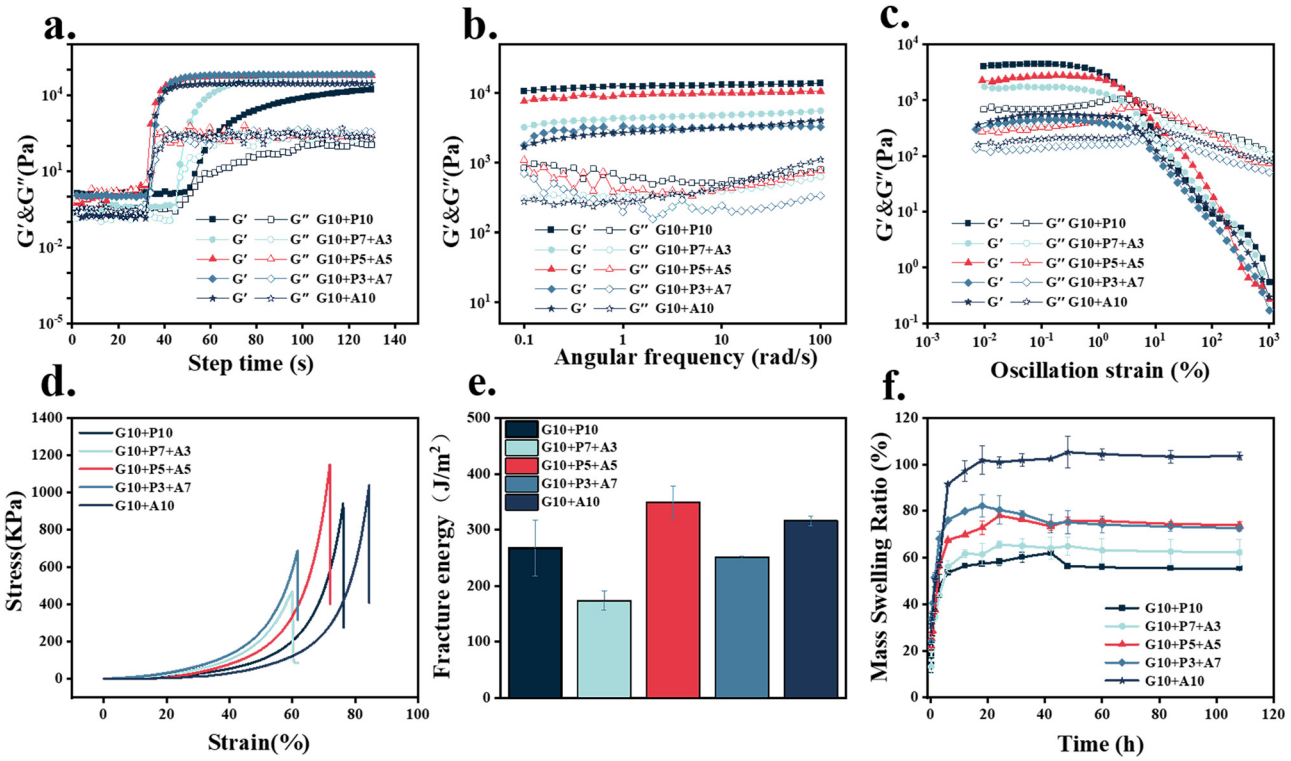

Fig. 3 Material evaluation and screening. (a) Time scan. (b) Frequency scan. (c) Strain scan. (d) Stress–strain curves for hydrogel compression tests. (e) Fracture energy of compression test. (f) Swelling test.

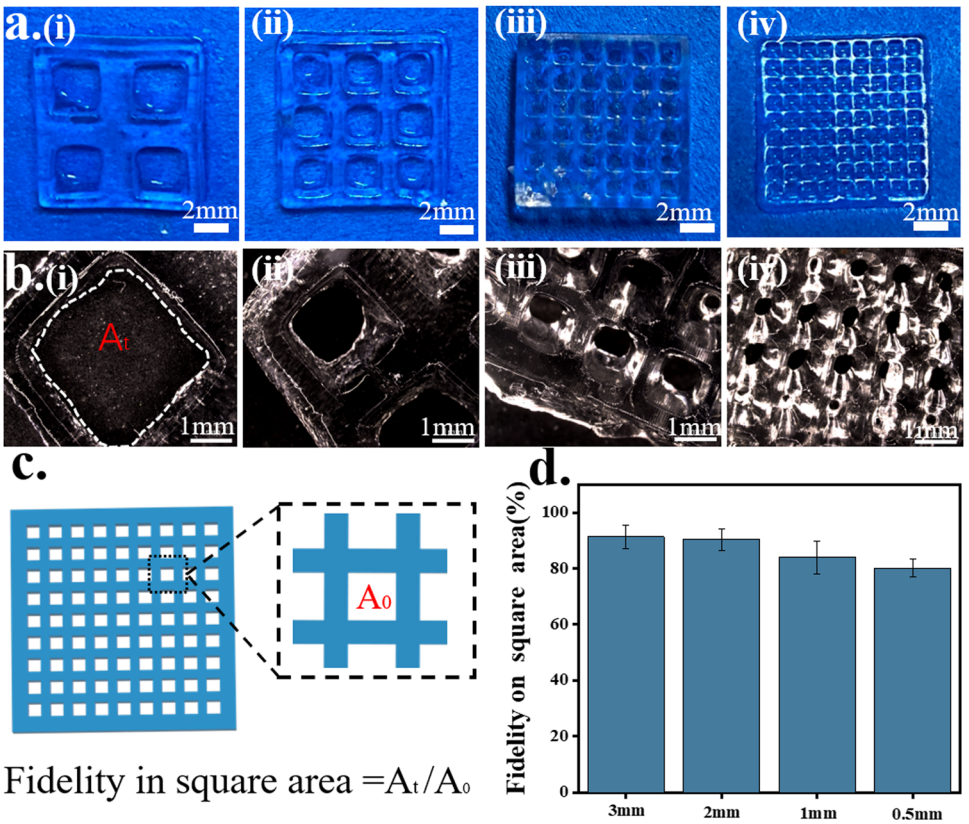

Fig. 4 Printability evaluation. (a) Porous holder printed with DLP, representing the printing resolution of this ink. (b) Optical diagram of the porous holder. (c) Calculation of printing accuracy. (d) Printing accuracy of different sizes of porous holders.

section. Student's *t*-test was used to assess differences between groups, and differences were considered statistically significant if $p < 0.05$. SPSS software was used for statistical analysis.

3. Results and discussion

3.1. Screening and evaluation of the light-curing inks

Fig. 2 shows the IR spectrum of PEGDA and the ^{1}H NMR of GelMA. Compared to PEG-2000, the newly generated characteristic absorption peak signal was found at 1723 cm^{-1} on the PEGDA-2000 IR curve (Fig. 2a), which is the absorption peak of the double bond (C═O), the characteristic peak of the PEG end group after esterification by chlorinated chloride. From the ^{1}H NMR of GelMA (Fig. 2b), it was found that compared with gelatin, GelMA showed two proton peaks, the acrylic acid proton peak (peak a + peak b, 5.5 ppm) and the methyl proton peak (peak d, 1.9 ppm) on the grafted methacrylamide. These two peaks gradually increased with an increasing degree of amino substitution, while the methylene proton peak (peak c, 2.8 ppm) on the unreacted lysine gradually weakened. In summary, PEGDA and GelMA were successfully synthesized. The degree of substitution of PEGDA-2000 was 83.5% as determined by ^{1}H NMR (Fig. S1, ESI†). The degree of amino substitution of GelMA-H was 97.33%. Through mechanical tests on PEGDA composite hydrogels with different molecular weights (Fig. S2, ESI†), it was shown that PEGDA with a molecular weight of 2000 has a higher fracture energy. To pursue high mechanical strength and 3D printing efficiency, PEGDA (M_w = 2000) and GelMA-H were used in subsequent experiments.

Rheological and mechanical tests were used to evaluate and screen the light-curing inks. The time scan of the light-curing process (Fig. 3a) showed that the higher the content of AAM in the light-curing inks, the faster the photocrosslinking rate. When the concentration of AAM in the hydrogel exceeded 5 wt%, the increase in the photocrosslinking rate was not significant. The results of the frequency sweep (Fig. 3b) showed that the energy storage modulus of samples G10 + P5 + A5 and G10 + P10 were relatively higher (10^4 Pa) than other samples. Therefore, sample G10 + P5 + A5 had both high elastic modulus and a fast photo-crosslinking rate. The strain sweep (Fig. 3c) results demonstrated that the 1% strain used in the frequency sweep test was in the LVE. The stress–strain curves of compression tests (Fig. 3d) and the calculation of the fracture energy (Fig. 3e) showed that the sample G10 + P5 + A5 required the largest energy to fracture, which reached 349 J m^{-2}. Good viscoelasticity and mechanical properties during the adhesion of octopus could attenuate the effect of negative vacuum pressure on the structure of octopus suction cups. Therefore, the sample G10 + P5 + A5 was chosen for all subsequent experiments.

The swelling of different samples (Fig. 3f) reached swelling equilibrium in 5 hours. With the increase in AAM concentration,

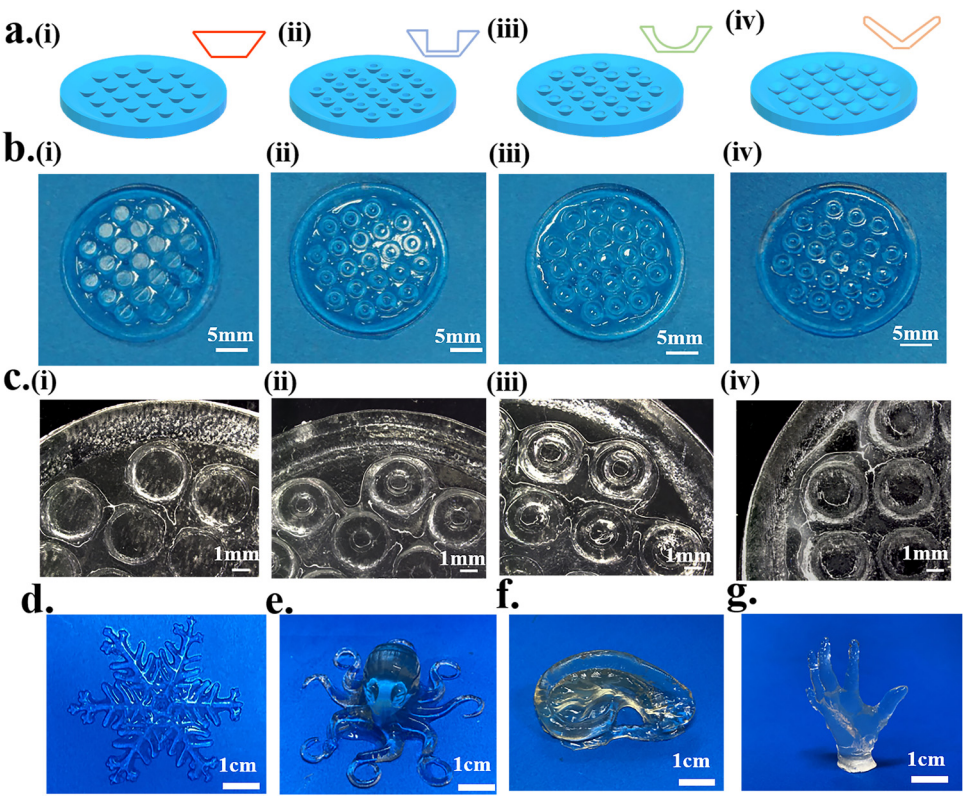

Fig. 5 Print of octopus-bionic suction cups. (a) Four different octopus bionic patch models, (i) circular table type, (ii) cylindrical hole type, (iii) hemispherical perforated type, (iv) conical hole type. (b) and (c) Optical pictures of different octopus-bionic patches. Complex printed structures ((d) snowflake, (e) octopus, (f) ear, (g) hand of free genius).

the swelling ratio of the sample gradually decreased. The higher the concentration of AAM, the higher the cross-link density inside the hydrogel. Compared with 200–300% of GelMA, G10 + P5 + A5 had a lower swelling ratio of 80%, which could ensure the structural stability of the patterned hydrogel patch obtained by DLP 3D printing in a liquid phase environment. As a trauma dressing, it had the ability to absorb tissue exudate.

3.2. Printability characterization

A mesh model and complex model were selected to evaluate the printability and printing accuracy of light-curing inks (Fig. 4). Mesh models with square holes of different sizes were constructed by DLP 3D printing (Fig. 4a). For the mesh model, the printing accuracy was obtained from the ratio of the void area of the actual printed product to that of the model (Fig. 4c). When the mesh size reached 500 μm × 500 μm, the square–hole structure could still be printed clearly (Fig. 4b) with up to 80% fidelity (Fig. 4d). The results demonstrated that the light-curing inks had good printability, and the printing conditions were also explored for the subsequent preparation of bionic patches.

Four different structures of the octopus-bionic patch models, namely, the circular table type, cylindrical hole type, hemispherical perforated type and conical hole type, were constructed by CAD software (Fig. 5a). These four structures of octopus-bionic patches were obtained by DLP (Fig. 5b, c, and S3, ESI†). As can be seen from the optical images, the patches were structurally intact. The fidelity was obtained by the ratio of the actual printed sucker bottom area to the theoretical area of the model, and it was found that the fidelity of the four structures of the octopus-bionic patch could reach 85% (Fig. S6, ESI†). In addition, the light-curing inks could also print complex models such as snowflakes (Fig. 5d), octopus (Fig. 5e), ears (Fig. 5f) and the hand of free genius (Fig. 5g). The snowflake outline was clear, and the octopus tentacles were intact which further proved that the light-curing ink G10 + P5 + A5 had good printability.

3.3. Adhesion

The adhesion properties of the octopus-bionic patches with different structures were compared and analyzed. From the force-time curves during the adhesion test (Fig. 6b), it could be

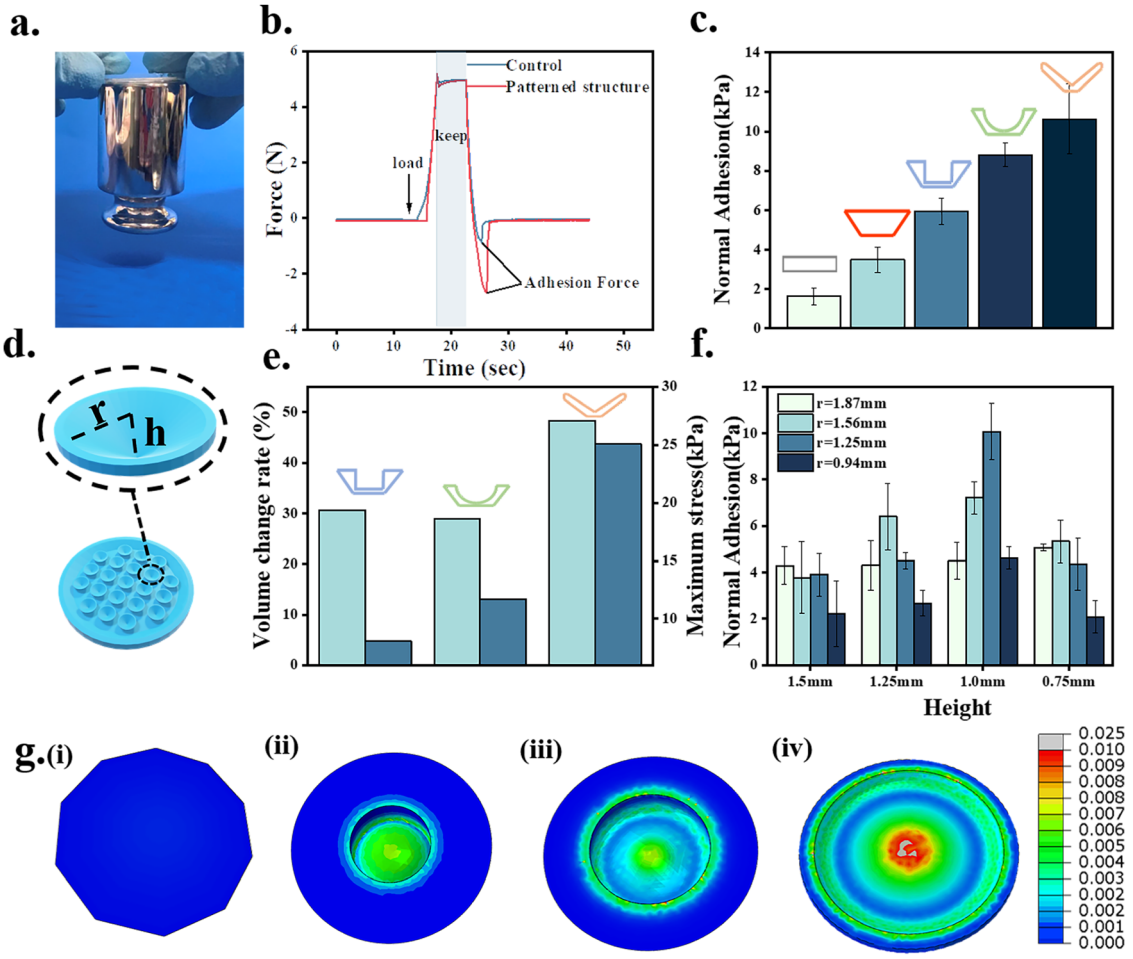

Fig. 6 (a) Schematic diagram of octopus bionic patch adhesion. (b) The curve of adhesion force with time. (c) The adhesion strength of patches with different structures. (d) Bionic suction cup model conical hole structure. (e) Simulated and calculated structures of different suction cup structures. (f) The adhesion strength of different-sized patches. (g) Stress clouds for finite element analysis of different suction cup structures, unit: MPa.

seen that the patches were first subjected to a preload force of 5 N, and then the adhesion force was generated. From the normal adhesion strength results of different structures, it was found that the octopus-bionic patch with a conical hole structure had the best adhesion (Fig. 6c), and the normal adhesion strength was up to 10.63 kPa, while the normal adhesion strength of the octopus-bionic patch with the circular table structure was only 3.49 kPa. The octopus-bionic patch with a conical hole structure had a cavity inside compared to the octopus-bionic patch with a circular table structure, the negative pressure was generated in the cavity part when the adhesion force was generated. The octopus-bionic patch with a round table structure had only the effect of the capillary force contributing to adhesion. The results showed that the adhesion force mainly came from the negative vacuum pressure generated by the suction cup structure. Meanwhile, the effect of the internal suction cup size on the adhesion of the patch was investigated (Fig. 6f). The results showed that the best adhesion of the patch was achieved when the radius of the hollow part of the internal suction cup was 1.25 mm and the height was 1 mm. If the size of the hollow part of the internal suction cup was too large or too small, it affected the liquid discharge and led to the reduction of negative pressure difference and adhesion. The screened octopus-bionic patch supports a weight of 200 g in the normal direction (Fig. 6a).

From the finite element analysis (Fig. 6e and g), the maximum stresses for the different structures corresponding to the normal adhesion were obtained. Loads of equal magnitude were applied to different structures to calculate the fluid cavity volume change between the suction cup structure and the skin, simulating the drainage effect of the suction cup structure. The results showed that the volume change rate of the fluid cavity with a conical hole type was the largest, the drainage effect was the best, and the negative pressure difference and adhesion were also the best. The theoretical results of the finite element analysis corroborated the actual experimental conclusions. It is worth noting that the volume change rate of the fluid cavity of the suction cup structure with a cylindrical hole type was slightly higher than that of the hemispherical perforated-type structure, while its normal adhesion strength was lower than that of the hemispherical perforated-type structure. This was mainly due to the hemispherical perforated-type structure having more stress on the edges, resulting in more friction, better sealing and higher adhesion strength.

To investigate the adhesion performance of the octopus-bionic patch on dry and different wetted surfaces, four liquids (water, 75% ethanol, 4 wt% gelatin, and simulated body fluids) were selected to wet the interface, and the adhesion strength was measured in comparison with the dry interface (Fig. 7b). It was found that the adhesion strength of the octopus-bionic patch was 1.68 kPa on the dry interface. In contrast, the octopus-bionic patch had better adhesion in a humid environment, and the different wetting solutions had little effect on the adhesion strength of the final octopus-bionic patch. When negative pressure was created inside the suction cup, the liquid

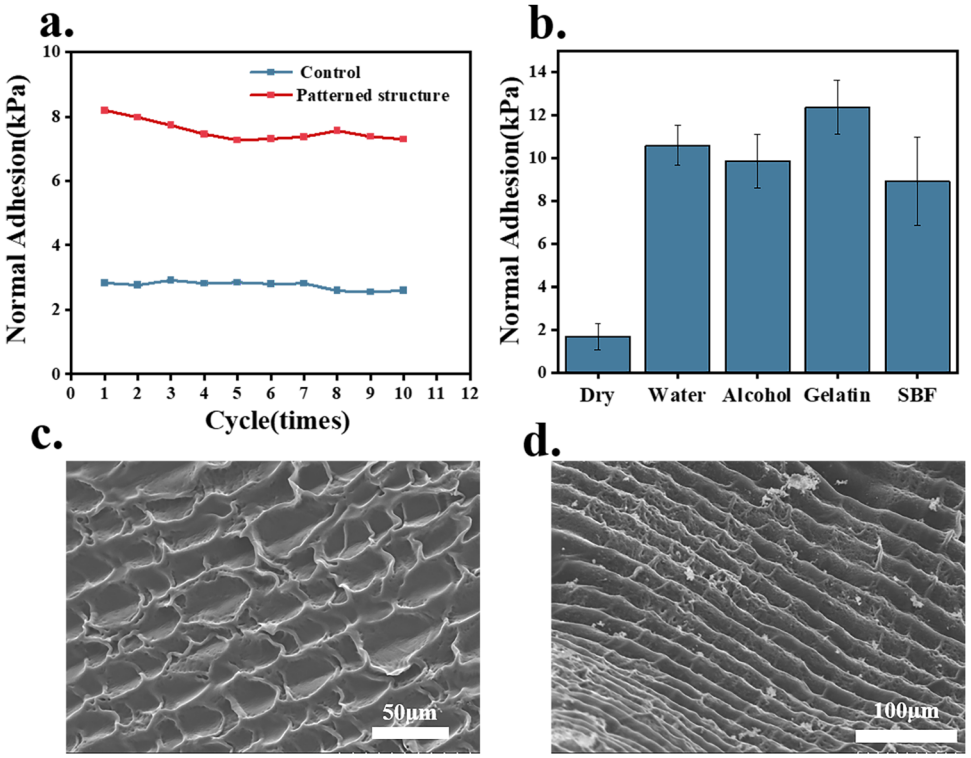

Fig. 7 (a) Cyclic adhesion testing on water-soaked pork skins, control: flat structure; patterned hydrogel: patch with conical perforated circular table structure. (b) Adhesion test with different surface conditions. (c) and (d) Scanning electron micrographs of 3D-printed constructed octopus-bionic patches at different magnifications.

molecules at the interface could prevent the entry of external fluids and help maintain the negative pressure. This also proved that the adhesion force of the octopus-bionic patch mainly came from the negative vacuum pressure, and a small part of the adhesion force came from the capillary force. Cyclic adhesion tests were used to explore the recyclability of the octopus-bionic patches (Fig. 7a and Fig. S5, ESI†). It was verified that after 10 cycles of adhesion and debonding, the octopus-bionic patch still had good adhesion, indicating that the patch can be recycled. The adhesion of the octopus-bionic patch tended to decrease slightly with the increase of repeated adhesion times, which was mainly due to the loss of moisture at the interface, resulting in the reduction of the sealing performance of the suction cup structure.

The octopus sucker was composed of a tightly arranged three-dimensional array of muscles with muscle fibers in three main directions: radial muscles across the wall, circular muscles surrounding the sucker, and transverse muscles perpendicular to the circular and radial muscles.[17,18] Surface roughness and microtopography were created due to the layer-by-layer deposition process of DLP printing. According to the SEM images of the hydrogel patch, the rough topography on the surface of the hydrogel patch resembled the valleys on the inner surface of the octopus sucker (Fig. 7 c and d). The roughness and microstructure of the hydrogel patch surface could enhance the friction of the suction cup and improve the sealing performance. In microstructure construction, DLP technology is beneficial to increase adhesion performance.

The peripheral structure of the octopus-bionic patch was further improved. The radial and circular grooves were constructed, respectively (Fig. 8a). The virtual simulation results showed that the stress distribution of the edge part of the patch decorated with the circular groove on the surface was uniform, and the maximum stress was 4.898×10^{-2} MPa (Fig. 8b), which created a good sealing effect. Compared with the patch modified with circular grooves on the surface, the stress distribution at the edge of the patch modified with radial grooves on the surface was not uniform, and stress concentration was prone to occur. The adhesion test results showed that the adhesion of the patch modified with the radial grooves was relatively weak, with a normal adhesion strength of 7.99 kPa, and the adhesion of the patch modified with an annular groove was the best (up to 12.53 kPa). In summary, the greater amount of liquid discharged, the formation of a negative pressure structure, and better sealing are the keys to the high adsorption force of the patch because the negative pressure structure could prevent gas or liquid from entering the chamber.

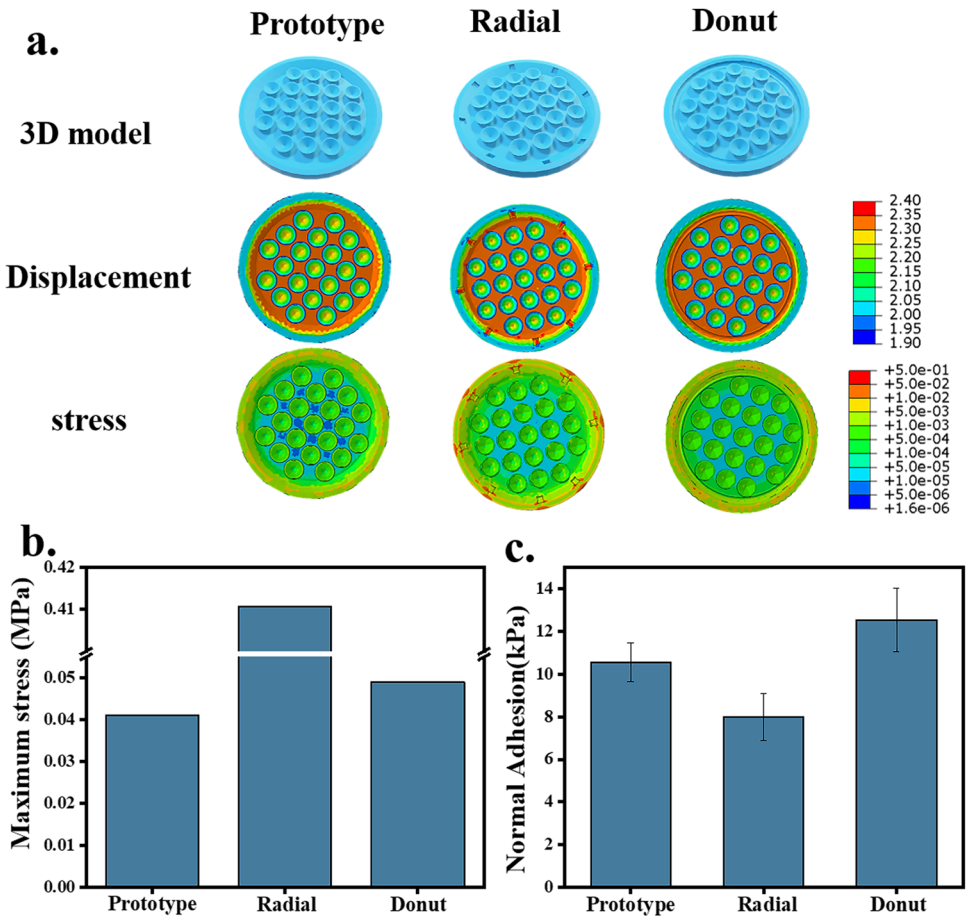

Fig. 8 (a) Finite element analysis of octopus release patches with different surface modifications; the unit of displacement is mm, the unit of stress is MPa. (b) Theoretical maximum stress. (c) Adhesion test with improved peripheral structure.

Inspired by the sucker structure of an octopus. Huang *et al.*[20] fabricated a GelMA-based patch by the template method with a normal adhesion of about 0.3 N cm^{-2} under a preload of 5 N. Baik *et al.*[8] developed a urethane acrylate-based patch with a normal adhesion strength of 12–13 kPa and a preload of 5 N by the template method. Under the same preload, the best adhesion of the octopus-bionic patch printed by DLP could reach 12.53 kPa. DLP printing can achieve personalized integrated molding, and also better simulate the rough structure of the octopus' surface, improve the adhesion of the octopus bionic patch and make its adhesion consistent with the patch based on urethane acrylate. In addition, the patch uses GelMA/PEGDA/AAM hydrogel, which can better simulate the extracellular matrix and has broad application prospects.

3.4. Personalized wound adhesion hydrogel patch

The 3D model of the octopus-bionic patch can be personalized according to the size and shape of the wound to better fit the wound and reduce material waste. The 3D model was constructed by CAD software (Fig. 9a), and the patches were constructed by DLP to match the model, *e.g.*, triangle (Fig. 9b(i)), quadrilateral (Fig. 9b(ii)), pentagram (Fig. 9b(iii)) and flowers (Fig. 9b(iv)).

The octopus-bionic patch had good adhesion and debonding properties, as well as good viscoelasticity. When the patch adhered to the pigskin, the octopus-bionic patch did not fall off the pigskin when the pigskin was bent or wiggled (Fig. 9c), indicating that the octopus-bionic patch could withstand large amplitude bending, which is suitable for wounds during sports. Through the cyclic stretching and compression of the patch material (Fig. S7, ESI†), the stress–strain curves of the first and subsequent cycles almost coincide, indicating that the hydrogel material had good stability and fatigue resistance, and could be used for flexible electronic equipment. The effects of the commercial patch (Comfeel® wound dressing) and the octopus-bionic patch on the skin tissue of the adhesion were further evaluated and compared (Fig. 9d). The results showed that the octopus-bionic patch did not cause secondary damage to the wound, while the commercial patch caused damage to the mucosa after debonding (the area indicated by the arrow is the secondary wound caused by the destruction). Since the adhesive force of the octopus-bionic patch mainly came from

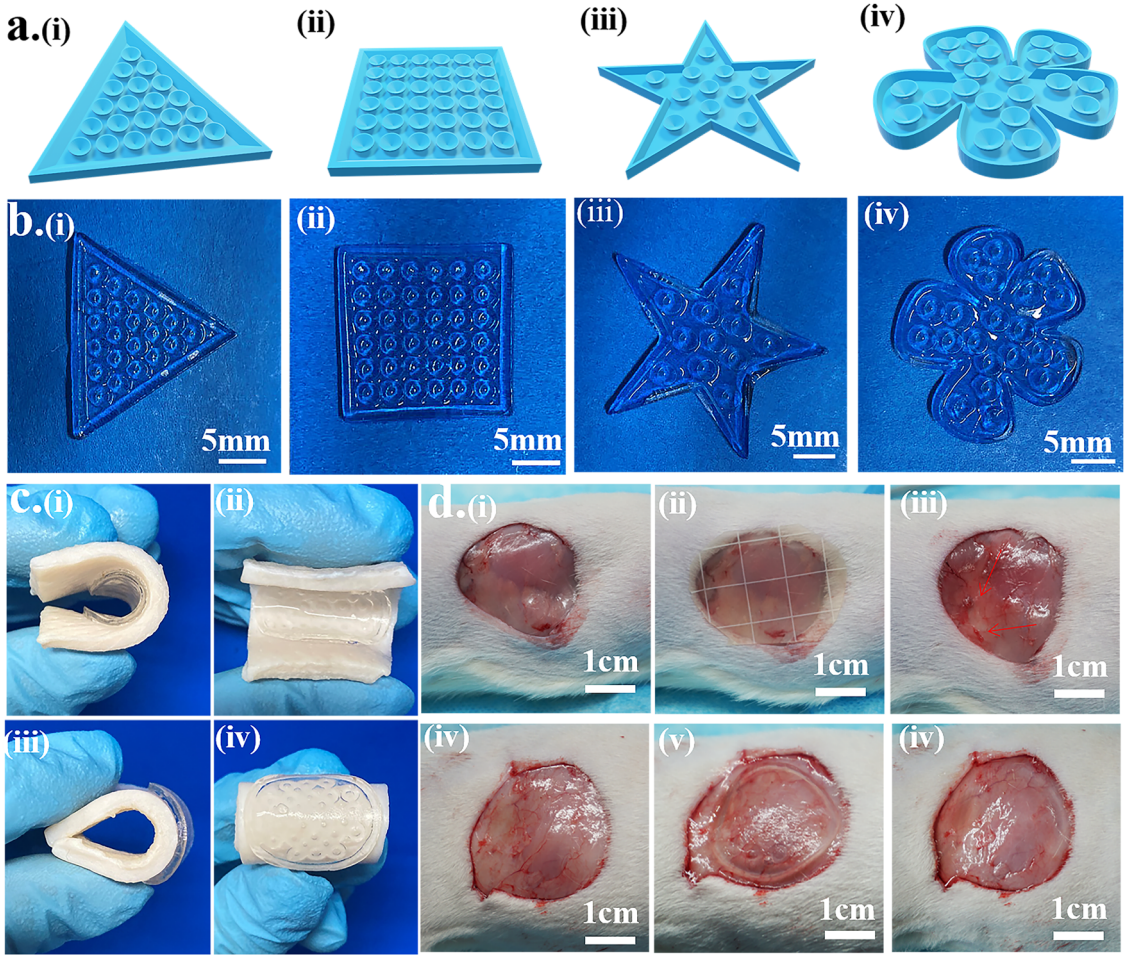

Fig. 9 Functional evaluation of the patch. (a) Personalized patches: (i) triangle, (ii) quadrilateral, (iii) pentagram, and (iv) flower. (b) Optical image of octopus bionic patches in various shapes. (c) Bendability: inward bending (i) side view, (ii) front view; outward bending (iii) side view, (iv) front view. (d) Ease of adhesion release: commercial patch adhesion (i) before, (ii) in, (iii) after; octopus bionic patch adhesion (iv) before, (v) in, (vi) after.

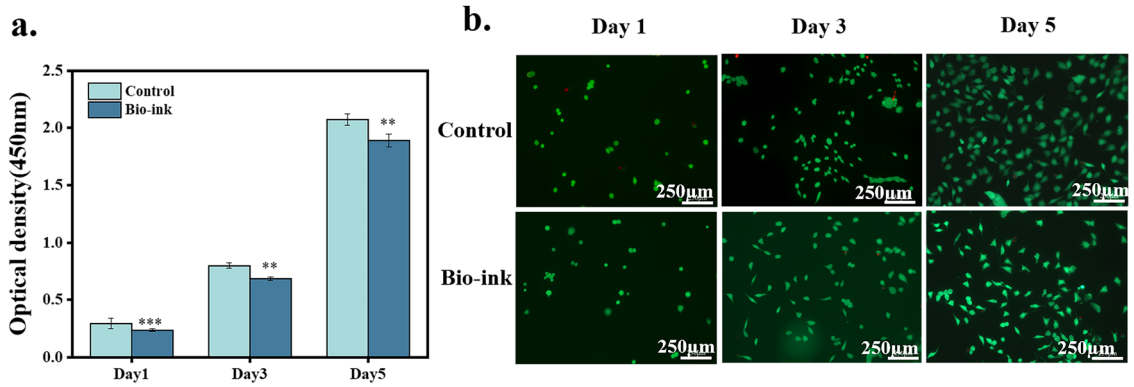

Fig. 10 Evaluation of the biocompatibility of the hydrogel. (a) CCK-8 cell proliferation assay of L929 cultured on the hydrogel surface on days 1, 3, and 5 (n = 6). (b) Live/Dead fluorescence images of L929 cultured on the hydrogel surface on days 1, 3, and 5.

the negative vacuum pressure, when the corner of the hydrogel patch was lifted and air entered the interface between the patch and the wound, the adhesive force disappeared, which facilitated debonding. In summary, the octopus-bionic patch has the versatility of being personalized, bendable and easy to debond.

3.5. Biocompatibility

The biocompatibility of the hydrogel was evaluated by cell proliferation and Live/Dead staining. The hydrogel was placed on the well plate and L929 cells cultured on the surface of the hydrogel were used as the experimental group. The culture plate was used as a control group. The optical density (OD) values were all increasing with the amount of culture time. The OD value of the experimental group was slightly lower than that of the control group. The ratio of the OD value of the group to the OD value of the control group was used to obtain the cell survival rate; the cell survival rate was higher than 80% (Fig. 10a). Furthermore, there were almost no dead cells in the experimental group (Fig. 10b), indicating that the hydrogel did not hinder the proliferation of cells and had good cytocompatibility.

4. Conclusions

In this study, a multifunctional GelMA/PEGDA/AAM hydrogel patch was constructed using the DLP printing technique by mimicking the sucker structure of the biological octopus. The hydrogel patch had good adhesion in wet environments, and the adhesion from negative vacuum pressure facilitated debonding. In addition, the DLP construction method endowed the octopus-bionic patch with personalized customization and a microstructure similar to that of the surface of the octopus. Good adhesion and debonding properties, biocompatibility, bendability, and easy debonding ability make this hydrogel patch promising for medical adhesives, smart climbing robots and biosensors.

Conflicts of interest

The authors declare that they have no known competing financial interests or personal relationships that could have appeared to influence the work reported in this paper.

Acknowledgements

This research was supported by the National Key Research and Development Program of China (Grant No. 2019YFD0901905) and the National Natural Science Foundation of China (Grant No. 31872758).

References

1 D. A. Paley and N. M. Wereley, *Bioinspired Sensing, Actuation, and Control in Underwater Soft Robotic Systems*, Springer, 2021.
2 Z. Xiao, Q. Zhao, Y. Niu and D. Zhao, *Soft Matter*, 2022, **18**, 3447–3464.
3 B. K. Ahn, *J. Am. Chem. Soc.*, 2017, **139**, 10166–10171.
4 C. Zhang, L. Xiang, J. Zhang, C. Liu, Z. Wang, H. Zeng and Z. K. Xu, *Chem. Sci.*, 2022, **13**, 1698–1705.
5 S. Baik, H. J. Lee, D. W. Kim, J. W. Kim, Y. Lee and C. Pang, *Adv. Mater.*, 2019, **31**, 1803309.
6 X. Fu, X. Zhang, D. Huang, L. Mao, Y. Qiu and Y. Zhao, *Chem. Eng. J.*, 2022, **431**, 133362.
7 A. H. Hofman, I. A. van Hees, J. Yang and M. Kamperman, *Adv. Mater.*, 2018, **30**, 1704640.
8 S. Baik, D. W. Kim, Y. Park, T.-J. Lee, S. Ho Bhang and C. Pang, *Nature*, 2017, **546**, 396–400.
9 M. K. Kwak, H. E. Jeong and K. Y. Suh, *Adv. Mater.*, 2011, **23**, 3949–3953.
10 L. Wang, Y. Hui, C. Fu, Z. Wang, M. Zhang and T. Zhang, *J. Adhes. Sci. Technol.*, 2020, **34**, 2275–2291.
11 Y. Wang, L. Zhang, Y. Guo, Y. Gan, G. Liu, D. Zhang and H. Chen, *Small*, 2021, **17**, e2103423.
12 D. W. Kim, S. Baik, H. Min, S. Chun, H. J. Lee, K. H. Kim, J. Y. Lee and C. Pang, *Adv. Funct. Mater.*, 2019, **29**, 1807614.
13 S. Chun, D. W. Kim, S. Baik, H. J. Lee, J. H. Lee, S. H. Bhang and C. Pang, *Adv. Funct. Mater.*, 2018, **28**, 1805224.
14 P. Rao, T. L. Sun, L. Chen, R. Takahashi, G. Shinohara, H. Guo, D. R. King, T. Kurokawa and J. P. Gong, *Adv. Mater.*, 2018, **30**, 1801884.
15 F. Tramacere, L. Beccai, M. Kuba, A. Gozzi, A. Bifone and B. Mazzolai, *PLoS One*, 2013, **8**, e65074.
16 J. J. Wilker, *Nature*, 2017, **546**, 358–359.

17 W. M. Kier and A. M. Smith, *Biol. Bull.*, 1990, **178**, 126–136.
18 W. M. Kier and A. M. Smith, *Integr. Comp. Biol.*, 2002, **42**, 1146–1153.
19 Y. Wu, X. Li, H. Tian, D. Wang, J. Zhang, L. Wang and J. Shao, *Adv. Funct. Mater.*, 2022, **33**, 2210562.
20 R. Huang, X. Zhang, W. Li, L. Shang, H. Wang and Y. Zhao, *Adv. Sci.*, 2021, **8**, 2100201.
21 S. Baik, J. Kim, H. J. Lee, T. H. Lee and C. Pang, *Adv. Sci.*, 2018, **5**, 1800100.
22 J. Kim, G. Zhang, M. Shi and Z. Suo, *Science*, 2021, **374**, 212–216.
23 H. Kumar, K. Sakthivel, M. G. Mohamed, E. Boras, S. R. Shin and K. Kim, *Macromol. Biosci.*, 2021, **21**, 2000317.
24 G. Ying, N. Jiang, C. Parra-Cantu, G. Tang, J. Zhang, H. Wang, S. Chen, N. P. Huang, J. Xie and Y. S. Zhang, *Adv. Funct. Mater.*, 2020, **30**, 2003740.
25 H. Shirahama, B. H. Lee, L. P. Tan and N.-J. Cho, *Sci. Rep.*, 2016, **6**, 1–11.
26 M. B. Browning and E. Cosgriff-Hernandez, *Biomacromolecules*, 2012, **13**, 779–786.
27 Y. Wang, Z. Li, M. Elhebeary, R. Hensel, E. Arzt and M. T. A. Saif, *Sci. Adv.*, 2022, **8**, eabm9341.
28 D. B. F. M. Hendriks, J. T. W. M. Van Eemeren, C. W. J. Oomens, F. P. T. Baaijens and J. B. A. M. Horsten, *Sking Res. Technol.*, 2003, **9**, 274–283.